communications engineering

Article

https://doi.org/10.1038/s44172-024-00326-w

AI-driven system for non-contact continuous nocturnal blood pressure monitoring using fiber optic ballistocardiography

Check for updates

Yandao Huang[1,2], Lin Chen[2], Chenggao Li[1], Junyao Peng[1], Qingyong Hu[1], Yu Sun[3], Hao Ren[4], Weimin Lyu[5], Wen Jin[3], Junzhang Tian[4], Changyuan Yu[5], Weibin Cheng[4] ✉, Kaishun Wu[2] ✉ & Qian Zhang[1] ✉

Continuous monitoring of nocturnal blood pressure is crucial for hypertension management and cardiovascular risk assessment. However, current clinical methods are invasive and discomforting, posing challenges. These traditional techniques often disrupt sleep, impacting patient compliance and measurement accuracy. Here we introduce a non-contact system for continuous monitoring of nocturnal blood pressure, utilizing ballistocardiogram signals. The key component of this system is the utilization of advanced, flexible fiber optic sensors designed to capture medical-grade ballistocardiogram signals accurately. Our artificial intelligence model extracts deep learning and fiducial features with physical meanings and implements an efficient, lightweight personalization scheme on the edge device. Furthermore, the system incorporates a crucial algorithm to automatically detect the user's sleeping posture, ensuring accurate measurement of nocturnal blood pressure. The model underwent rigorous evaluation using open-source and self-collected datasets comprising 158 subjects, demonstrating its effectiveness across various blood pressure ranges, demographic groups, and sleep states. This innovative system, suitable for real-world unconstrained sleeping scenarios, allows for enhanced hypertension screening and management and provides new insights for clinical research into cardiovascular complications.

Compared to snapshot blood pressure measurement, continuous blood pressure monitoring provides additional information and insights for screening, diagnosis, and treatment of cardiovascular and cerebrovascular diseases[1,2]. Recently, nocturnal hypertension has been reported to be a significant risk factor for cardiovascular incidents[3–6]. Nocturnal blood pressure has a better prognostic value than daytime blood pressure[3,7], and it can independently predict the risk of mortality and cardiovascular events[5,8]. The significance of nocturnal blood pressure control for hypertension management has been widely acknowledged. However, most clinically adopted continuous blood pressure monitoring methods, such as intra-arterial catheters and cuff-based sphygmomanometers, present significant limitations. These include invasiveness, discomfort, and the potential to disrupt sleep, posing challenges for long-term patient compliance and accurate nocturnal blood pressure monitoring[9].

Recent advancements in wearable technology and non-invasive sensors have improved the ability to monitor blood pressure non-invasively, continuously, and comfortably. Estimating blood pressure accurately using wearable cuffless devices remains a formidable challenge[10–14]. The prevalent method for blood pressure estimation in wearable technology is based on the Moens-Korteweg equations[15–18], which reveal the relationship between pulse wave velocity (PWV) and arterial stiffness to in driving blood pressure. Non-invasive measurement of PWV is feasible over a known distance.

[1]Department of Computer Science and Engineering, Hong Kong University of Science and Technology, Hong Kong, China. [2]The Hong Kong University of Science and Technology (Guangzhou), Guangzhou, Guangdong, China. [3]Department of Cardiac Intensive Care Unit, Guangdong Second Provincial General Hospital, Guangzhou, Guangdong, China. [4]Institute for Healthcare Artificial Intelligence, Guangdong Second Provincial General Hospital, Guangzhou, Guangdong, China. [5]Department of Electrical and Electronic Engineering, The Hong Kong Polytechnic University, Hong Kong, China. ✉e-mail: chwb817@gmail.com; wuks@hkust-gz.edu.cn; qianzh@cse.ust.hk

However, blood vessel length is difficult to measure, and researchers typically use pulse arrival time (PAT) and pulse transit time (PTT) as an approximation of PWV. For example, PAT can be measured as the time difference between the R-peak of an electrocardiogram (ECG) and the foot of a peripheral photoplethysmogram (PPG) waveform. While promising, this methodology overlooks the intrinsic dynamic variations in the contractility of peripheral vascular smooth muscle (SM)[16,19] during specific conditions, such as administration of vasoactive pharmaceuticals[20,21] and circadian rhythms[22]. Therefore, this approach requires frequent calibration (e.g., every 5 min to 2 h[23–27]) to guarantee accuracy. In addition, users must wear devices that require frequent recharging, degrading the convenience and user compliance.

Ballistocardiogram (BCG) was initially observed by Gordon on a weighing scale in 1877[28]. The BCG signals document the ballistic forces due to the abrupt ejection of blood into the great vessels during each heartbeat, encompassing breathing and body movement. It measures the body's overall micro-movements triggered by the forces associated with heart contraction, thereby providing insights into the overall performance of the circulatory system. Kim et al.[29] mathematically built the BCG genesis model, where the genesis of BCG signals is interpreted as the blood pressure gradient difference between the ascending and descending aorta. This finding underpins the rationale for using BCG to infer continuous blood pressure. In addition, BCG is reflected by the aorta, which is less affected by the SM contractility compared to the PTT-based method[16,19].

In this article, we present a lightweight AI system that can continuously, contactlessly, and accurately monitor nocturnal blood pressure using high-quality medical-grade BCG signals. As shown in Fig. 1a, b, our system includes a specialized flexible fiber optic sensor that can be deployed under the pillow for contactless sensing, and real-time BCG data is collected as the system input. Our AI system fuses both deep-learning features and hand-crafted fiducial features with physical meanings, and the pretrained model undergoes efficient and lightweight personalization on the edge device. The deep-learning features are extracted based on the U^{2}Net structure, which is good at capturing the salient and multi-scale features from the BCG waveform. We propose an automatic delineation algorithm to locate fiducial points of each BCG cycle and calculate fiducial features that incorporate cardiovascular domain knowledge. The system can also automatically recognize a subject's sleep posture, which is a critical factor in ensuring accurate nocturnal blood pressure measurement.

Our proposal was extensively evaluated in both open-source (40 subjects)[30] and self-collected clinical datasets (118 subjects), covering large blood pressure (BP) fluctuation ranges and large populations with dynamic demography. Our self-collected dataset is the largest BCG-BP dataset, which involves 85 subjects tested in the daytime and 33 subjects tested in nocturnal sleep scenarios without any constraint. Our system aims to deliver an effective, accurate, contactless BP monitor in real-world, unconstrained sleeping environments. It represents a breakthrough in nocturnal BP monitoring, offering a user-friendly, low-cost, and easy-to-use alternative to traditional methods. It not only revolutionizes the way to early screening and better management of hypertension and other cardiovascular diseases but also builds a foundation for innovative clinical research on some hypertension complications.

Results

Our nocturnal continuous blood pressure system integrates a medical-grade, high-fidelity BCG sensing hardware system and an AI software system infused with the physical characteristics for BP measurement. The hardware system is based on fiber optic sensing, primarily consisting of a laser emitter, step-index multimode fiber, and a photodiode receiver, which ensures the collected BCG signals are of high fidelity, and suitable for medical-grade applications. Furthermore, our sensor mat is flexible and biocompatible, ensuring user comfort, safety, and portability. It can be easily integrated into medical textiles and everyday items such as cushions, pillows, chairs, and beds.

As depicted in Fig. 1c, the AI software system encompasses several key components: (1) Data preparation, involving signal preprocessing of raw BCG data, segment-wise posture recognition, and delineation of fiducial points for each cardiac cycle; (2) Feature extraction, focusing on deriving both deep-learning representations and fiducial features that have physical meaning; (3) Edge computing, sharing model weights from the cloud-pretrained deep-learning model and inserting a lightweight machine learning algorithm as the regressor for personalized fine-tuning and BP inference; (4) Customized user interface, which establishes communication with the edge terminal via WiFi and provides real-time display of the user's vital signs data (see Supplementary Movie 1).

Flexible fiber optic BCG sensor

The circuit and block diagram of the fiber optic BCG sensing hardware system are depicted in Fig. 1d. It includes a Fabry–Perot (FP) laser diode (LD) as the light source, which emits at a wavelength of 1550 nm and a power of 3 mW. The photodetector (PD), utilizing an InGaAs PIN configuration, is capable of detecting light in the range of 850 to 1700 nm. A precision analog-to-digital converter (ADC) with one channel and 16-bit resolution is employed to sample BCG signals at a rate of 500 Hz. The system utilizes a high-performance microcontroller unit (MCU) featuring an ARM 32-bit Cortex-M4 CPU, which can operate at frequencies up to 168 MHz. This MCU manages the general-purpose input/output (GPIO) pins, supplying voltage to circuit components and transmitting ADC-sampled BCG data to the user interface. The entire circuit requires an external power supply of 5 V 1 A via USB. In practical use, the device consumes a maximum of only 0.32 W when fully operational. Figure 1e plots the sample waveforms from time-synchronized ECG, BCG, and finger cuff-based pulse sensors.

An exploded view in Fig. 2a highlights the multi-layered structure of the sensor mat. A section of step-index multimode silica optical fiber with a core diameter of 62.5 μm and numerical aperture (NA) of 0.275 is used as the sensing fiber. The bare fiber is wound and attached to a PET plastic film with a size of 270 mm × 450 mm × 0.3 mm in a certain pattern. A grid-shaped polyamide fiber with a 1.1 mm opening (Λ) is covered over the optical fiber, acting as the deformer to bend the fiber core. Two medical-grade semi-transparent silicone elastomers (300 mm × 500 mm × 1 mm) are pressed together and enclose the sensing fiber in between. Finally, we craft an outer covering made of polyester material, which fits snugly against the silicone layer, completely encasing the entire sensor mat. Figure 2b shows that the deformer causes periodic (Λ) fiber deformation change by an amount ΔX, inducing micro-bending loss. Figure 2c shows a typical plot of sensor output P as a function of weight F. The force is applied uniformly over the area of 0.05 m^2 within the sensor mat. Figure 2d shows the sensor sensitivity curve as a function of weight based on the fitting curve of Fig. 2c. More details regarding micro-bending fiber optic theory and sensor characteristics are illustrated in Supplementary Note 1.

Datasets and model training

The first dataset is the Kansas dataset[30], which is an open-source dataset developed by researchers at Kansas State University. This open-source dataset features a variety of synchronized multimodal physiological signals, including BCG, ECG, PPG, and arterial blood pressure (ABP) waveform. The BCG signals within this dataset were obtained using a combination of four electromechanical film (EMFi) sensors under the mattress and four load cells positioned under the foot of the bed. To ensure accurate time alignment and consistent data sampling at 1000 Hz, both sensor types were integrated using a National Instruments 9220 analog input module. Data were collected from 40 subjects (17 males) with ages ranging from 18 to 65 years. Four of the subjects have cardiovascular-related conditions. Overall, the systolic pressure ranges from 58.7 to 187.0 mmHg, and the diastolic pressure ranges from 44.5 to 101.0 mmHg. Individually, the systolic pressure dynamics (max-min) varied from 11 to 46 mmHg, and the diastolic pressure dynamics varied from 5 to 27 mmHg. In total, over 4.5 h of data were collected.

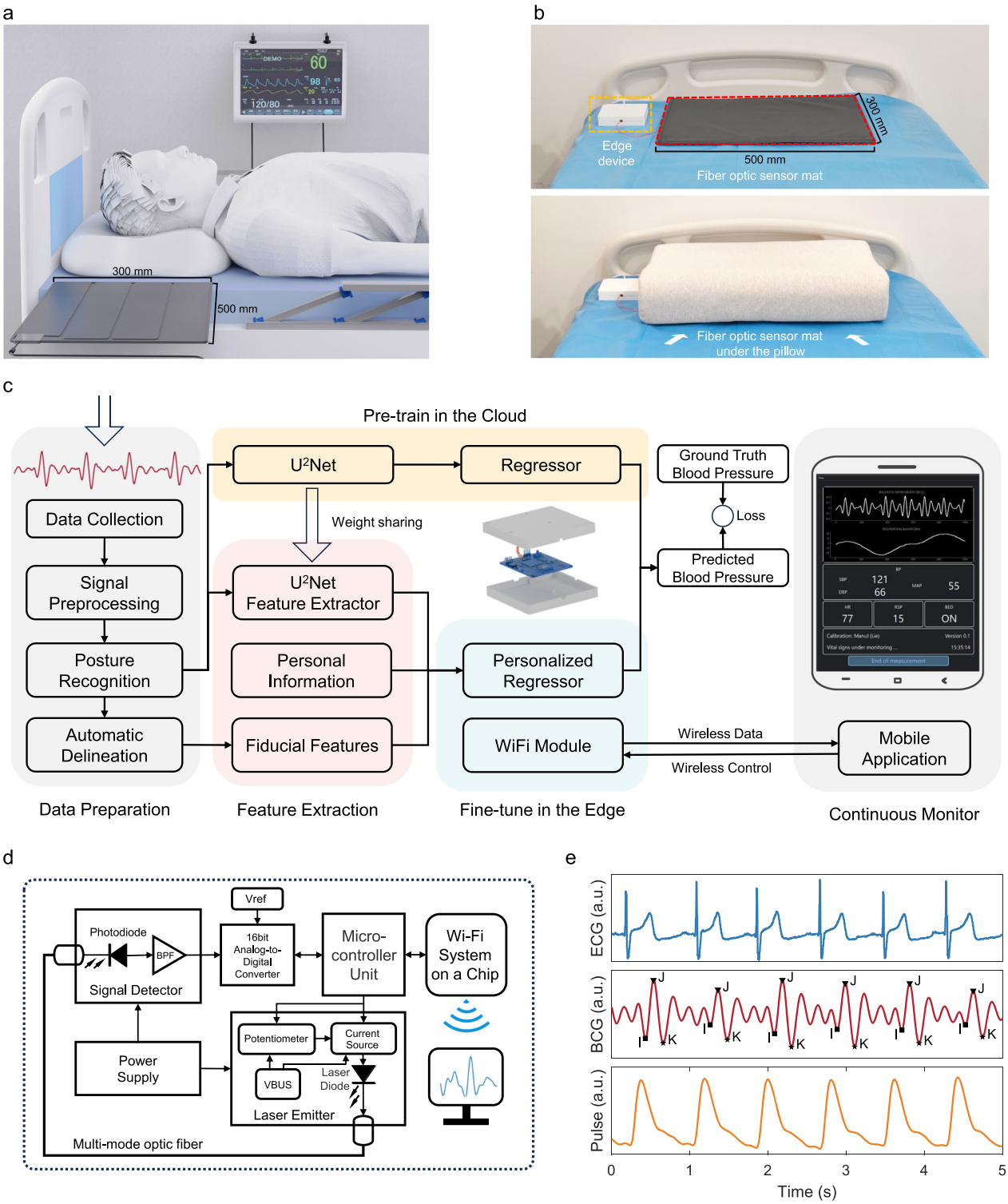

Fig. 1 | The concept and system overview of non-contact continuous nocturnal blood pressure (BP) monitor. a A typical use scenario of our system, where the fiber optic sensing mat is placed beneath the user's pillow. **b** The system prototype deployed in the real world. **c** Block diagrams of the system. The data preparation stage preprocesses ballistocardiogram signals for posture recognition and fiducial point delineation. The feature extraction stage extracts meaningful features for training a base model. The base model will be directly deployed in the edge device, while a Random Forest model is trained as the personalized regressor to infer the BP in the edge. The customized user interface enables WiFi connectivity for live vital sign monitoring. **d** System's circuit and block diagram. The fiber optic sensing capability primarily builds upon a laser emitter, a section of multimode fiber, and a photodiode receiver. **e** Sample waveforms from time-synchronized electrocardiogram (ECG), ballistocardiogram (BCG), and finger cuff-based pulse sensors. BPF is a bandpass filter, Vref is reference voltage, VBUS is USB power voltage, and a.u. is arbitrary units.

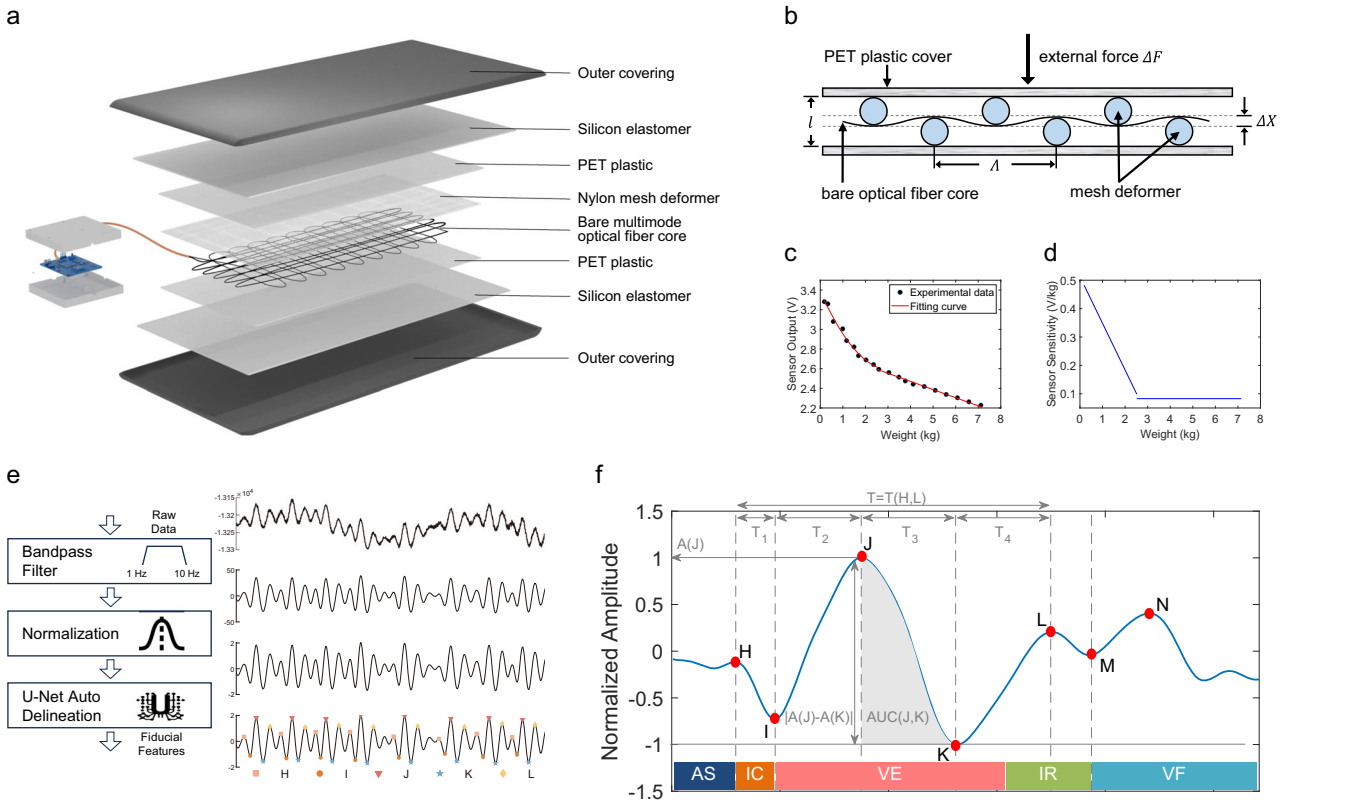

Fig. 2 | Flexible fiber optic BCG sensor design and the extraction of hand-crafted fiducial features. a Exploded schematic illustration of the constituent layers: a bare multimode optical fiber core, a grid-shape nylon deformer, two polyethylene terephthalate (PET) plastic films as core cover, two silicon elastomers encapsulation layers, and a fitting polyester outer covering. **b** schematic of the microbend fiber sensor. **c** Sensor output as a function of weight. **d** Sensor sensitivity as a function of weight. **e** Illustration of fiducial points labeling. **f** Sample illustration of five types of fiducial features: extremum—$A(J)$, displacement—$|A(J) - A(K)|$, time interval—$T(H, L)$, time ratio—T_1/T, and area under the curve—$AUC(J, K)$. The periodic contraction (systole) and relaxation (diastole) of the heart can be illustrated into five major stages: (1) atrial systole (AS), (2) isometric ventricular contraction (IC), (3) ventricular ejection (VE), (4) isometric ventricular relaxation (IR), and (5) ventricular filling (VF).

The second dataset is a self-collected dataset from the Department of Cardiac Intensive Care Unit at Guangdong Second Provincial General Hospital. The self-collected dataset consists of two subgroups: a daytime group and a nocturnal group. The first group, consisting of 85 subjects, was collected during the day while the subjects lay awake in bed. The second group comprises 33 subjects, each of whom records data for a minimum of 6 h during uncontrolled, natural sleep periods. Supplementary Table 1 describes the demography of these two groups. Supplementary Figs. 3–6 plots BP variation ranges for each subject in the self-collected daytime and nocturnal dataset. Blood pressure changes in response to different body postures, awake and sleep states during measurement[31,32]. The daytime group accounted for the validation of the system performance in the supine posture but did not actually reflect the nocturnal blood pressure during sleep states. Therefore, we use the nocturnal group to complement this issue.

We deployed the proposed flexible fiber optic BCG sensor under the pillow to accurately measure BCG signals at 500 Hz. The FDA-approved Caretaker device[33] (Caretaker Medical LLC, Charlottesville, VA, USA) was used as a ground truth device that provided beat-to-beat non-invasive blood pressure, ECG, and other vital signs data. Synchronization between the BCG sensor and ground truth device was achieved via network time protocol (NTP).

Figure 2e shows the high-level schematic for extracting fiducial points from the input raw BCG signals and visualizes the output results of each step. The subject-wise raw data were first processed through a 1–10 Hz bandpass filter and then normalized to a uniform scale. Then, a 5-s sliding window with a 1-s frameshift was applied to obtain samples. Each 5-s segment was fed into U-Net for fiducial point delineation. Based on fiducial points, we calculated five types of fiducial features: extremum, displacement, time interval, time ratio, and area under the curve (AUC), as illustrated in Fig. 2f. The description of the full list of 44 fiducial features is given in Supplementary Table 2. More details on how we preprocess the BCG signals to get fiducial features are shown in Supplementary Figs. 13–17.

To prevent data leakage, we performed leave-one-out cross-validation for model evaluation, which guarantees that no sample of the testing subject is used in the pre-training stage. As shown in Supplementary Fig. 10, the parameters of the pretrained U^2-Net encoder were frozen and directly deployed in the edge device through weight sharing. As for the personalization stage, we replaced the multi-layer perceptron (MLP) layers with the Random Forest (RF) regressor and incorporated personal information (gender, age, height, and weight) and fiducial features for personalization. We only used the data from the first 30 seconds to train the RF-based personalization module.

Clinical study in daytime dataset

We first evaluate our system using the Kansas dataset and our self-collected daytime dataset. Figure 3a, b depicts the overall correlation and Bland–Altman plots for the estimated SBP and DBP. For the Kansas dataset, correlation plots reveal correlation coefficients of 0.90 for SBP and 0.92 for

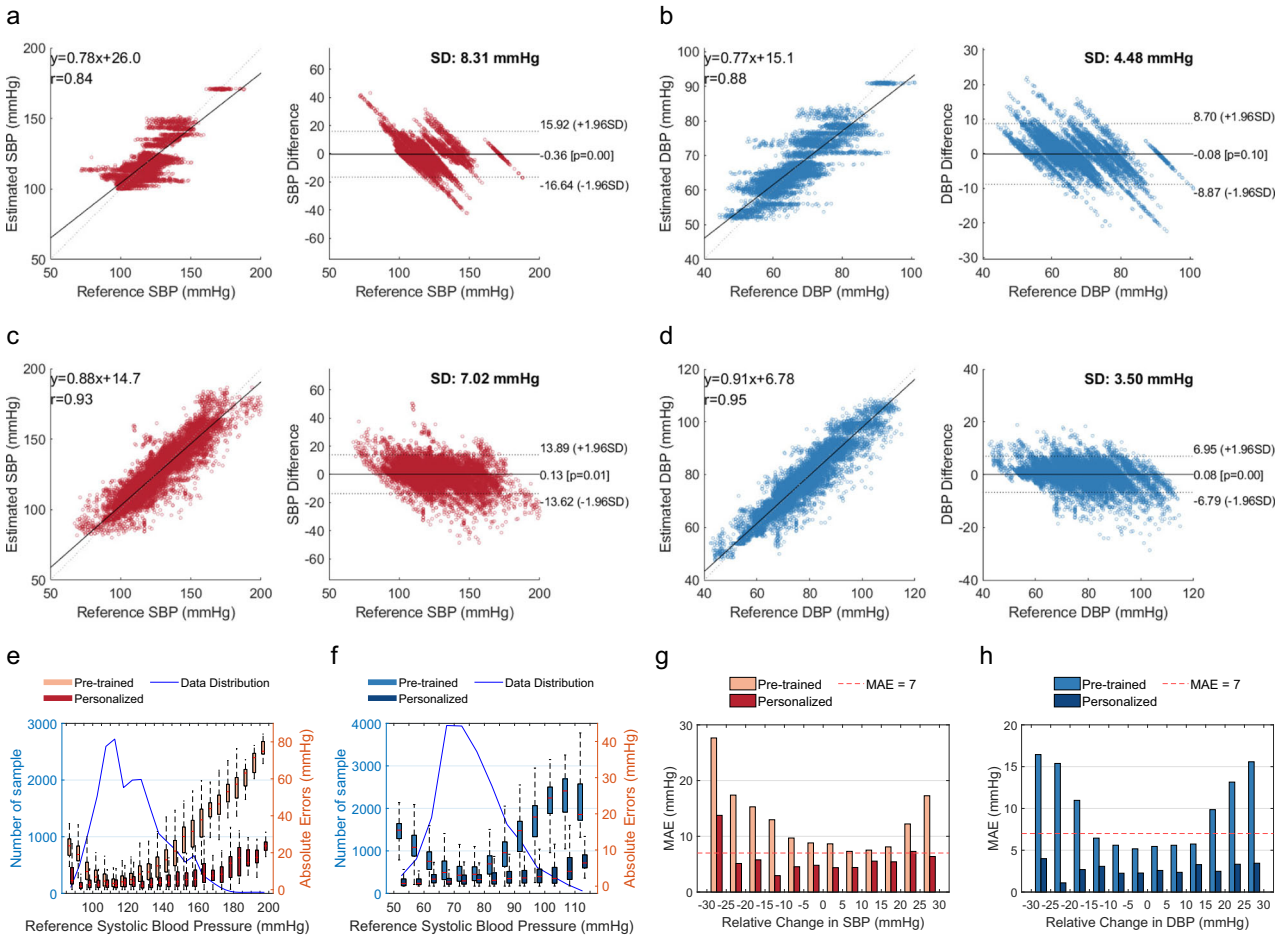

Fig. 3 | Performance of the clinical study in the daytime dataset. a, **b** The correlation and Bland–Altman plots for the open-source dataset, where **a** is for systolic blood pressure (SBP) results, and **b** is for diastolic blood pressure (DBP) results. **c**, **d** The correlation and Bland–Altman plots for the self-collected daytime dataset, where **c** is for SBP results, and **b** is for DBP results. **e**, **f** Mean absolute error (MAE) for different blood pressure levels before and after personalization, where **e** is for SBP results, and **f** is for DBP results. The blue line indicates the number of samples, while the box plots indicate absolute errors. Error bars represent the range of data within 1.5 times the interquartile range (IQR) from the first quartile (Q1) to the third quartile (Q3). **g, h** The distribution of MAE of all subjects at different BP change intervals, where **g** is for SBP results, and **h** is for DBP results. The red line indicates MAE = 7 mmHg. SD is the standard deviation of mean error.

DBP when compared with reference BP values. This indicates a strong correlation between the estimated and reference BP values. The Bland–Altman plots show that the mean error (ME) and standard deviation (STD) are -0.19 ± 8.31 mmHg for SBP and -0.04 ± 4.48 mmHg for DBP. Meanwhile, the dotted lines represent the limit of agreement (LOA)[34], defined as $ME \pm 1.96 \times STD$. LOA of SBP and DBP are $[-16.43, 15.92]$ mmHg and $[-8.87, 8.70]$ mmHg, respectively. Supplementary Fig. 7 plots the comparison results between the estimated BP and reference BP values using testing samples from all the subjects in the open-source dataset.

In our daytime dataset (Fig. 3c, d), the predicted SBP and DBP show correlation coefficients of 0.93 and 0.95 with reference BP, respectively. The ME and STD are 0.13 ± 7.02 mmHg for SBP, 0.06 ± 3.50 mmHg for DBP. LOA of SBP and DBP are $[-13.62, 13.89]$ mmHg and $[-6.79, 6.95]$ mmHg, respectively. Figure 3e, f details the mean absolute error (MAE) for different BP ranges with a step size of 5 mmHg with respect to reference BP. The fine-tuned model obtains an overall MAE of 4.78 mmHg for SBP and 2.40 mmHg for DBP. Figure 3g, h plots the MAE histogram at different intervals of BP changes (from -30 to 30 mmHg with a step size of 5 mmHg) compared to the calibration baseline BP. The performance is accurate (MAE $\leq$7 mmHg) for BP changes from baseline between -25 and $+30$ mmHg. Supplementary Fig. 8 plots the comparison results between the estimated BP and reference BP values using testing samples from all the subjects in our daytime dataset.

Supplementary Table 3 summarizes the international clinical requirement of ANSI/AAMI/ISO standard[35], IEEE 1708 standard[36,37], and British Hypertension Society (BHS) protocol[38]. Supplementary Table 4 provides the overall performance regarding metrics of these standards and lists the detailed results for various subpopulations. Overall, the daytime results demonstrate that our system meets the ANSI/AAMI/ISO standard and achieves the Grade A rating according to IEEE 1708 and BHS criteria.

Continuous nocturnal blood pressure monitoring

Our nocturnal experiment was conducted under natural sleep scenarios without any constraints on sleep posture. To reduce variation caused by body posture, current clinical guidelines[39] recommend that BP should be measured in supine posture (UP). Therefore, we designed the sleep posture recognition modules to ensure accurate BP measurement during the proper postural condition. In this section, we first validate the effectiveness of posture recognition by using the daytime dataset, where data of four sleep postures (namely, UP, DOWN, LEFT, RIGHT) were collected. Figure 4a plots the confusion matrix of classification accuracy regarding 85 persons. On average, the classification accuracy of four postures is 86.2%. Figure 4b shows the receiver operating characteristic (ROC) curves obtained under different thresholds. The average area under the curve value is 0.967. In practice, we only consider the recognition of supine posture (i.e., UP) as the standard BP measurement posture. The binary classification accuracy

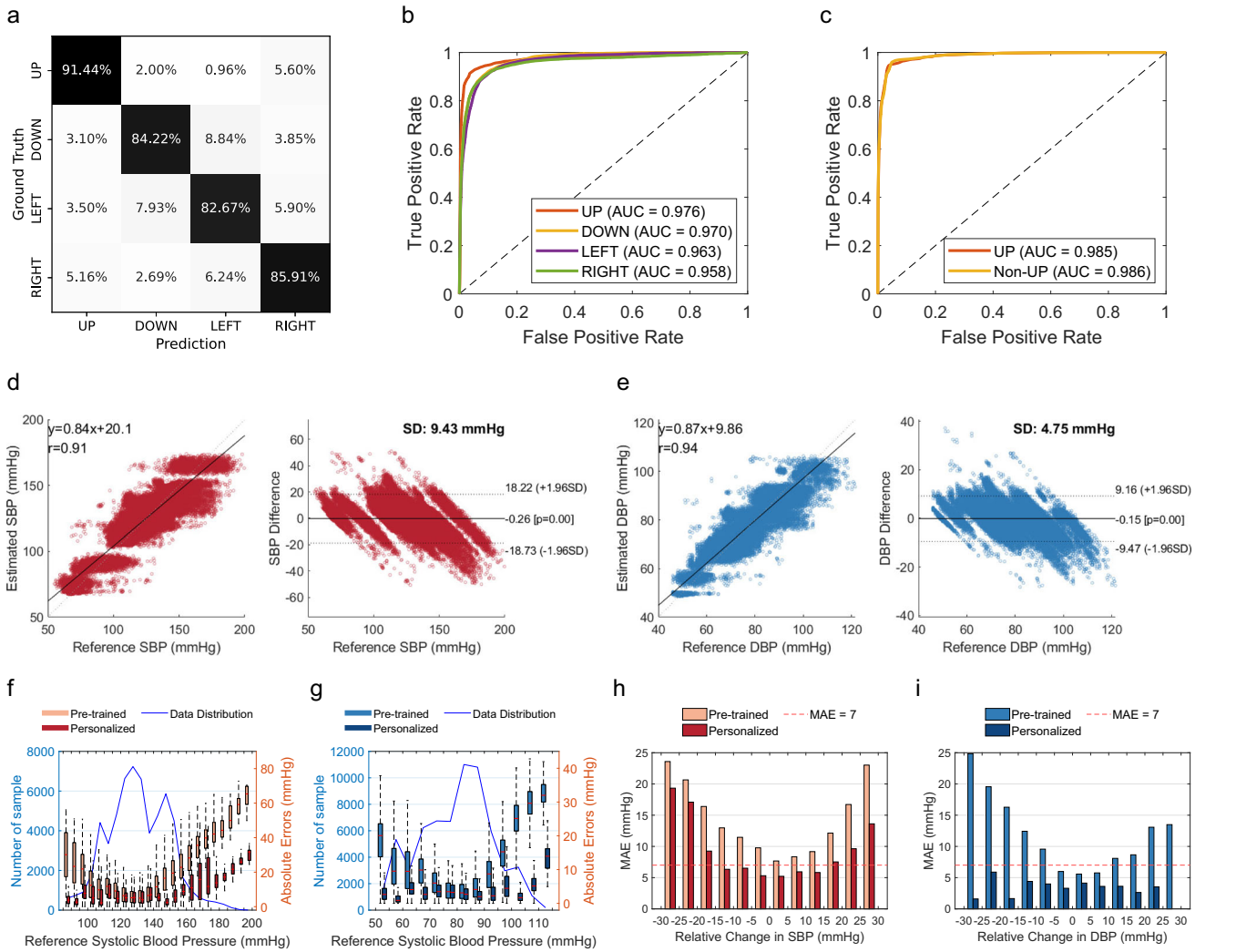

Fig. 4 | Performance of the clinical study for continuous nocturnal blood pressure monitoring. a Confusion matrix of sleep posture prediction during the day, grouped by four different sleep postures. **b**, **c** Receiver operating characteristic curves for four postures classification (**b**), and binary posture classification during the night (**c**). **d**, **e** The correlation and Bland–Altman plots for the self-collected nocturnal dataset, where **d** is for systolic blood pressure (SBP) results, and **e** is for diastolic blood pressure (DBP) results. **f**, **g** Mean absolute error (MAE) for different blood pressure levels before and after personalization, where **f** is for SBP results, and **g** is for DBP results. The blue line indicates the number of samples, while the box plots indicate absolute errors. Error bars represent the range of data within 1.5 times the inter-quartile range (IQR) from the first quartile (Q1) to the third quartile (Q3). **h**, **i** The distribution of MAE of all subjects at different BP change intervals, where **h** is for SBP results, and **i** is for DBP results. The red line indicates MAE = 7 mmHg. SD is the standard deviation of mean error.

reaches 94.1% when tested with whole-night sleep data. As shown in Fig. 4c, the AUC values of ROC curves are 0.985 for supine posture (UP) and 0.986 for non-supine posture (non-UP).

When a subject is stable in the supine posture, the system will infer his nocturnal BP continuously. As shown in Fig. 4d, e, the Pearson correlation coefficient for nocturnal sleeping SBP and DBP is 0.91 and 0.94, respectively. Compared to daytime, the nocturnal dataset exhibits a higher estimation error, with mean errors and standard deviations of −0.26 and 9.43 for SBP, −0.15 and 4.75 for DBP. Figure 4f, g plots the MAE for different BP ranges grouped by reference BP. On average, the MAE for SBP and DBP estimation is 6.90 mmHg and 3.46 mmHg, respectively. Figure 4h, i plots the MAE histogram at different intervals of BP changes (from −30 to 30 mmHg) compared to the calibration baseline BP. The performance is accurate for BP changes from baseline between −15 and +20 mmHg, where MAE is less than 7 mmHg. Beyond this range, the error significantly increases. We plot all subjects' data and compare the estimated BP and reference BP throughout the night in Supplementary Fig. 9. Detailed statistics for various BP and age levels in the nocturnal dataset are given in Supplementary Table 5.

Ablation study

We conducted extensive experiments to evaluate the effectiveness of key designs within the system. In this section, we examine the impact of different fiducial feature subsets, the personalization module, and the posture recognition module. The corresponding results are presented in Table 1.

First, we explore the impact of employing different fiducial feature subsets (Task 3–7). We discover that incorporating personal information (Task 4) or fiducial features (Task 5) reduces the standard deviation of SBP by 0.36 (4.55%) and 0.65 (8.22%), respectively. Fusing all the deep learning and hand-crafted features with domain knowledge (Task 6) further reduces the standard deviation of SBP by 0.89 (11.25%) due to the deep interaction among more features in the model. The results validate that the features have different degrees of physical meanings related to BP inference.

Subsequently, we assess the impact of the personalization module (Tasks 1–2, 4–5, and 6–7). For the open-source dataset, the personalization reduces the standard deviation of SBP from 14.57 to 6.60. For the daytime dataset, the personalization reduces the standard deviation of SBP from 14.20 to 7.02. For the nocturnal dataset, the personalization reduces the

Table 1 | Ablation study

Task	Dataset	PR	BCG	PI	FF	PM	Diastolic blood pressure				Systolic blood pressure			
							Corr	MAE	ME	STD	Corr	MAE	ME	STD
1	OS	✓	✓	✓	✓	✓	0.84	3.31	-0.36	8.31	0.90	5.97	-0.18	6.60
2	OS	✓	✓	✓	✓	×	0.11	7.70	−1.80	10.27	0.30	11.59	−3.60	14.57
3	Self-day	–	✓	–	–	✓	0.93	2.78	0.15	4.06	0.91	5.42	0.32	7.91
4	Self-day	–	✓	✓	–	✓	0.94	2.66	−0.04	3.88	0.92	5.25	0.03	7.55
5	Self-day	–	✓	–	✓	✓	0.95	2.56	0.15	3.69	0.92	5.03	0.30	7.26
6	Self-day	–	✓	✓	✓	✓	0.95	2.41	0.08	3.50	0.93	4.78	0.13	7.02
7	Self-day	–	✓	✓	✓	×	0.56	7.17	−1.00	9.44	0.62	10.68	−3.80	14.20
8	Self-night	✓	✓	✓	✓	×	0.06	11.90	−0.08	15.34	0.14	19.11	−0.10	24.92
9	Self-night	✓	✓	✓	✓	✓	0.94	3.46	−0.15	4.75	0.91	6.93	−0.27	9.48
10	Self-night	×	✓	✓	✓	✓	0.83	5.74	−1.10	7.64	0.75	11.53	−2.10	15.22

Investigation of the impact of different feature subsets, the personalization module, and the sleep posture recognition module. PR for posture recognition, BCG for ballistocardiogram, PI for personal information, FF for fiducial features, PM for personalization module, OS for open-source dataset, Self-Day for self-collected daytime dataset, Self-Night for self-collected nocturnal dataset, DBP for diastolic blood pressure, SBP for systolic blood pressure, Corr for Pearson correlation coefficient, MAE for mean absolute error, ME for mean error, STD for standard deviation of mean error.

standard deviation of SBP from 24.92 to 9.48. This reveals the effectiveness and necessity of using lightweight samples for personalization.

Finally, we evaluate the impact of the posture recognition module (Task 9–10). We see that when turning off the posture recognition and inferring the BP using all the nocturnal data, the performance degrades by a lot. This occurs as the testing set includes significant data collected in non-lying postures. The fluctuations and changes in blood pressure collected in these poses are elusive, and the training set does not contain samples of these poses, so the AI model cannot accurately infer the blood pressure under non-standard posture, which causes poor estimation results.

Model interpretability

Figure 5a, b present scatter plots generated using t-distributed stochastic neighborhood embedding (T-SNE) techniques. T-SNE is a statistical method for visualizing high-dimensional data by reducing it to two or three dimensions. The points in Fig. 5a, b represent the fused features in two-dimensional space, with color gradients from dark to light indicating varying blood pressure values for specific samples. The visualization reveals that our AI model learns the non-linear mapping from extracted features to BP values.

Additionally, we utilize interpretable hand-crafted feature sets for performance optimization. In this analysis, we employ Shapley Additive exPlanations (SHAP), known for effectively illustrating the impact of individual features on each sample. This method not only highlights the influence of these features on the model but also clearly indicates whether their effects are positive or negative. Figure 5c, d present summary plots interpreting the overall samples for SBP and DBP, respectively. In these plots, each row corresponds to a specific feature, and the horizontal axis represents the SHAP values. Individual points on these plots denote samples, where the color indicates the feature value: red for higher values, and blue for lower values. The breadth of the distribution in these areas signifies the extent of influence each feature has. More influential features are positioned at the top. Notably, the four most important features are $|A(J)-(L)|$, $|A(J)-A(K)|$, $|A(H)-(J)|$, and $A(L)$ for SBP estimation, while that for DBP estimation are $T(H,I)/T$, $|A(J)-A(L)|$, $T(H,J)$, $|A(H)-A(J)|$. Kim et al.,[40] indicate that the "H-J interval" (i.e., $|A(H)-(J)|$) represents aortic PTT, a well-known surrogate of DBP, and "J-K amplitude" (i.e., $|A(J)-A(K)|$) represents aortic outlet, a surrogate of pulse pressure. Supplementary Note 2 provides more detailed explanations on how BCG fiducial features represent the heart's geometric deformation and correlate with blood pressure waves.

Discussion

This study marks an advancement in blood pressure monitoring. We develop an AI system leveraging high-sensitivity fiber optic sensors and integrating advanced deep-learning algorithms for non-invasive, continuous nocturnal blood pressure monitoring. Our contribution lies in the system's ability to capture high-fidelity, medical-grade ballistocardiographic signals and infer precise blood pressure readings. This technical innovation represents a leap forward in both the methodology and application of blood pressure monitoring.

The implications of our findings are multifaceted. Firstly, our system enables early screening, aiding in the timely identification and intervention of prehypertension and also isolated nocturnal hypertension. Secondly, it plays a crucial role in the management of chronic diseases, particularly in the adjustment of antihypertensive medication and the assessment of drug efficacy, by facilitating long-term monitoring and personalized management. Lastly, our system, being contactless, detects real nocturnal BP readings, which is pivotal in uncovering the truth of hypertension complications, such as hypertension with sleep apnea. With the revelation of true nocturnal blood pressure profiles, a sound foundation is provided for lots of clinical research.

Looking ahead, our system's potential applications are extensive. It can be seamlessly integrated into various everyday items like pillows, mattresses, chairs, and cushions. This integration offers the potential of passive, continuous health monitoring in an individual's home, providing valuable feedback to healthcare providers. Such a deployment could revolutionize the way we approach health monitoring and management at a personal level.

Despite its advancements, this study has limitations. Nocturnal blood pressure measurements exhibit greater variability than that in the daytime, which raises questions about the system's precision in comparison to medical-grade devices. Furthermore, the absence of a longitudinal study means yet to determine the duration for which a single calibration remains valid. The necessity for calibration also presents a challenge, steering future research toward the development of calibration-free systems. Future studies should focus on enhancing the accuracy of nocturnal blood pressure measurements and extending the longevity of calibration stability, to make the system more robust and user-friendly.

The significant error increase at the data's outermost edges may be attributed to a straightforward reason: the model struggles to make accurate predictions at these extremes because it lacks sufficient training data in these ranges. As depicted in Figs. 3f, g, 4f, g, there is a sharp decline in the quantity of data available for abnormal BP levels. This is attributable to the study design and falls within normal dynamic variation for subjects.

In conclusion, while our system represents a step forward in blood pressure monitoring technology, ongoing research, and development are essential to address its current limitations and fully realize its potential in both clinical and home settings.

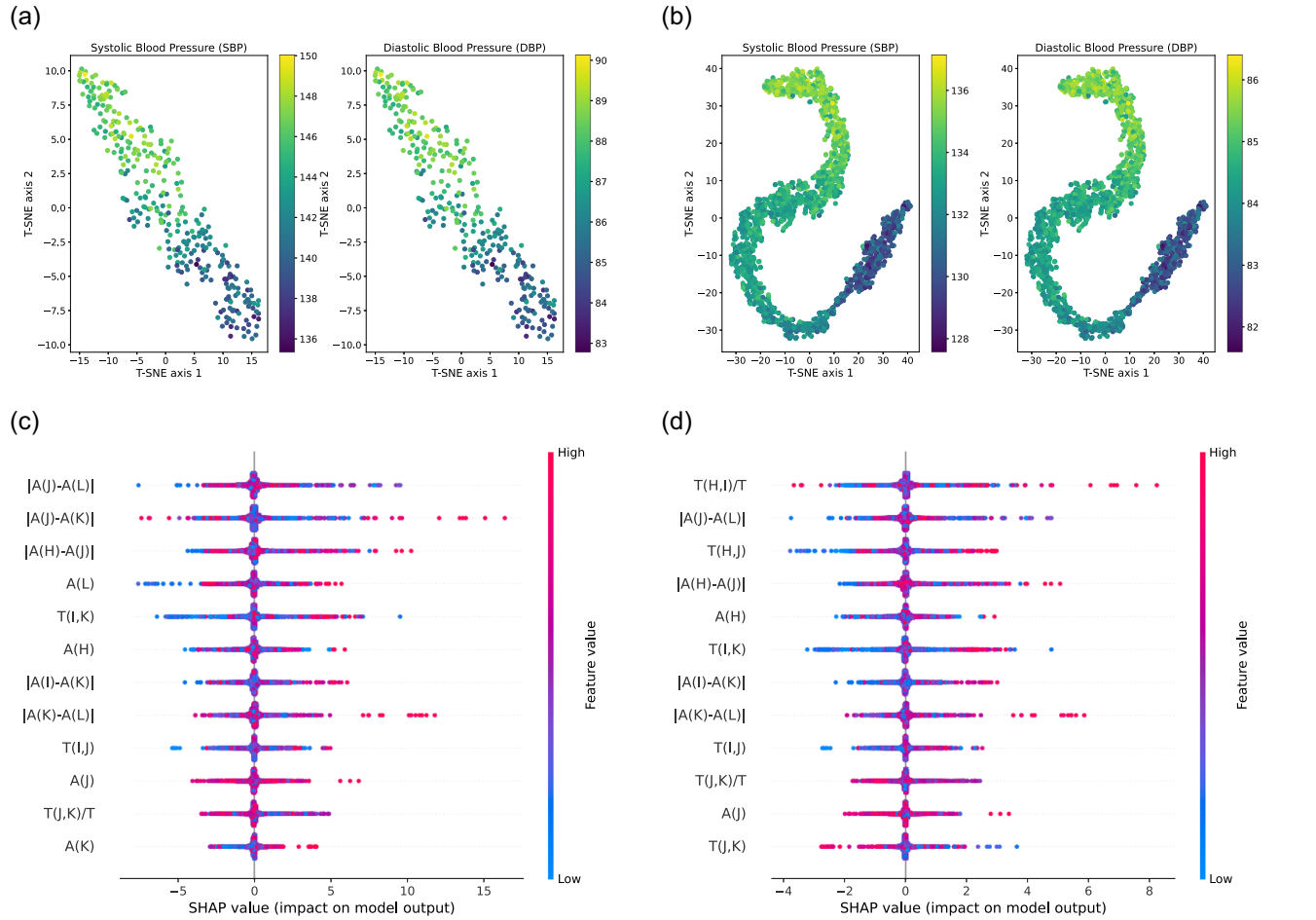

Fig. 5 | Interpretation of artificial intelligence model using T-SNE and SHAP analysis. a, **b** Scatter plot of extracted features after dimension reduction using t-distributed stochastic neighborhood embedding (T-SNE) techniques, where **a** uses daytime data, and **b** uses nocturnal data. **c**, **d** Feature important ranking using Shapley additive exPlanations (SHAP) analysis, where **c** is for SBP and **d** is for DBP.

Methods

Dataset collection

Initially, the study included 88 subjects in the daytime dataset and 40 subjects in the nocturnal dataset. Three patients were excluded from the daytime dataset and seven from the nocturnal dataset due to storage errors, missing channel data, and device disconnection. The inclusion and exclusion criteria are listed in Supplementary Note 3. A comprehensive demographic breakdown of the included subjects is presented in Supplementary Table 1.

The daytime data collection involves two sessions. The first session collects standard data, and the second session focuses on data from various sleeping positions. The specific procedure for the first session is as follows: A flexible fiber optic sensor is placed under the pillow, a Caretaker oximeter is clipped to the subject's right index finger, a Caretaker sleeve-type cuff is wrapped around the middle finger for beat-to-beat blood pressure measurements, and a Caretaker single-channel flexible wireless ECG patch is attached to the chest. After the sensors are properly fitted, the subject lies flat on the bed with arms resting by their sides. Clinical standard blood pressure is measured once with the cuff-based BP device, followed by device calibration according to the Caretaker's instructions. After the continuous blood pressure device is calibrated, the first standard data collection begins, lasting for 3 min. During the measurement, the subject is asked to breathe normally but not move their body. After the first collection, the subject stands up and immerses their left hand in ice water for 30 s to induce blood pressure fluctuations due to vasoconstriction. After 30 s, the subject lies back on the bed for the second standard data collection, also lasting for 3 min. Subsequently, the subject performs 1 min of squatting exercises to increase the heart rate. After the heart rate is elevated, they lie back on the bed for the third standard data collection, continuing for 3 min. After this, the subject stands up and rests before starting the second session. In the second session, the subject is required to lie still in various positions—flat, on the left side, on the right side, and prone—for 3 min each to collect data. At the end, medical personnel measure and record the subject's blood pressure in the lying position using a cuff blood pressure monitor.

For the nocturnal dataset, all subjects are required to sleep in the hospital bed for an entire night (from 10 p.m. to 6 a.m., ensuring at least 6 h of sleep data collection). Before falling asleep and after waking up, a medical personnel measures and records the subject's lying blood pressure using a cuff blood pressure monitor. Throughout the collection process, there is no restriction on the subject's sleeping position or behavior. An RGB camera is installed to annotate sleep postures.

The study protocol was reviewed and approved by the institutional review board of the Guangdong Second Provincial General Hospital (protocol no. 2023-KY-KZ-082-01). All subjects reviewed and signed the printed consent forms before participating in our study. No export of human genetic material or data in this study.

Data preprocessing. A sixth-order Butterworth bandpass filter, with cutoff frequencies of 1–10 Hz, is applied to remove respiratory and high-frequency noise from BCG signals. This ensures the data reflects cardiac-

related vibrations with high fidelity. To balance accuracy and computational efficiency, all data are downsampled and unified at a rate of 250 Hz. Then, the filtered signals will be normalized using Z-score normalization before input into the U-net automatic delineation. Supplementary Figs. 3–17 provide a long-term session of BCG signals to show how the signals are processed and get the fiducial points. The fiber optic sensor is highly sensitive. In some extreme cases, there are motion artifacts caused by body movements. Supplementary Figs. 15–17 illustrate how our system deals with noisy signals and gets precise fiducial points at the same time. It's worth mentioning that our U-net model is trained with standard BCG signals to automatically label the fiducial points, and the U-net model does not recognize the unseen noisy segment and will not label fiducial points on those parts, which helps us to eliminate the noisy segment from the input data.

Hardware design. The circuit's key components include (1) a microcontrol unit (STM32F407ZGT6, STMicroelectronics), (2) an analog-to-digital converter (ADS1146IPWR, Texas Instruments), (3) a Fabry–Perot laser (1550 nm, 3 mV), (4) an InGaAs PIN photodiode (850–1700 nm), (5) power management, (6) a WiFi system-on-a-chip (ESP8266, ESPRESSIF), and (7) a self-assembled fiber optic sensor mat.

Assembly of the sensor mat begins by spreading dual-sided silicone-acrylate adhesive (2477p, 3M) over one side of the PET film. Then, a section of bare step-index multimode silica optical fiber is wound over the PET film. A grid-shaped polyamide fiber film that is the same size as PET film is covered over the optical fiber. Another PET film layer covers the polyamide fiber film. Two medical-grade silicone elastomers (300 mm × 500 mm × 1 mm) were pressed together using external clamps and allowed to cure, thereby creating a sealed enclosure with sensing fiber in between. In the end, an outer covering made of leather material, which fits snugly against the silicone layer, completely encases the entire sensor mat.

Model implementation. The AI system is built on three learning-based models: (1) a ResNet-LSTM structure for sleep posture detection, (2) a U-Net for automatic delineation, and (3) a U^2-Net structure integrated with RF-based personalization for real-time continuous non-contact BP inference.

Sleep posture detection. Blood pressure readings are known to vary with different postural conditions. Clinically, to obtain precise blood pressure measurements, patients are required to be in a supine position, lying flat. Our system should specifically identify periods when the user is in a supine position. Owing to the 3D structure of the aorta, the BCG waveforms exhibit significant differences when users adopt various sleeping postures[41,42]. Therefore, we train a general neural network based on the ResNet-LSTM structure, which takes 10-s BCG signals as input and outputs the current postural condition. This neural network model utilizes a three-layer ResNet to extract global structural representations from the BCG signals and a single-layer LSTM to capture the temporal dependency between heartbeat cycles.

Automatic delineation. The automatic delineation algorithm aims to identify the fiducial points (H, I, J, K, and L) in each BCG cycle. We take advantage of deep-learning techniques to automatically label the fiducial points. We adopt the efficient and lightweight U-Net structure with 1D convolutional layers in our neural network[43]. The trained neural network takes one-channel pre-processed BCG signals of 10 s as input and outputs six-channel softmax probability scores. Each channel has the same length. One of the channels indicates the probability score of background sample points, while the other channels correspond to each fiducial peak. This subnetwork is trained using fiducial peak annotations from human experts.

BP inference. The most essential part is the AI model for continuous BP inference. As shown in Supplementary Fig. 10, the training of cNBP-Net has two stages: pre-training in the cloud and personalization in the edge. In the pre-training stage, we use a large number of labeled samples from different users to train a base model, as shown in Supplementary Fig. 11. The base model has a U^2-net structure as the deep-learning features extractor and two MLP layers as the BP regressor. Compared to traditional U-Net, which only uses convolutional layers for feature extraction, the U^2-net adopts U-units (Supplementary Fig. 12) to extract multi-scale features while preserving critical signal characteristics. A U-unit first uses a plain convolutional layer for local feature extraction, where the input signals are transformed into an intermediate representation with C_{out} channels. Then, a U-shape symmetric encoder-decoder structure with a height of $L = 6$ gradually downsamples the intermediate representations and encodes them into multi-scale features. Finally, the output of a U-unit is a summation that fuses local features and multi-scale features. Overall, the U^2-net is made up of multiple U-units, 2x downsampling operations, and 2x upsampling operations. Specifically, there are 5 U-units in the U^2-net encoder and 4 U-units in the U^2-net decoder. In the training stage, the base model will not only predict the BP values but also output the reconstructed BCG signals. The Huber loss function is used to evaluate regression loss between BP prediction and ground truth BP. The MSE loss function is used to evaluate the reconstruction loss between reconstructed BCG and BCG input. The joint optimization of these two loss functions enables the neural networks to learn general feature representations while preserving necessary BCG characteristics in the code.

During the personalization stage, only the trained U^2-net encoder is deployed in the edge device, and the MLP layers will be replaced by an RF regressor. The RF regressor takes both deep-learning features and hand-crafted features into consideration and learns the non-linear mapping from fused features to blood pressure labels. When meeting an unseen target user, a small portion of labeled samples will be used to personalize the RF regressor. In practice, a user can measure their ground truth BP as data labels using a cuff-based sphygmomanometer.

Using RF as a regressor has the following advantages: Firstly, unlike MLP, RF does not require back-propagation, therefore the computational load is significantly less. The model can be easily trained in a low-cost and lightweight edge device. Secondly, machine learning models require less amount of training samples compared to deep-learning models. Moreover, RF is an ensemble learning algorithm and it is based on bootstrapping, making it less likely to overfit. In practice, users can measure their blood pressure several times using a cuff-based blood pressure monitor to obtain ground truth annotations for their BCG data. This is done to initialize and personalize their continuous blood pressure prediction model. Then, a regular re-calibration (typically every 7–28 days) is needed to maintain the model accuracy.

Statistical analysis. Analysis of sensor data was performed in Python 3.8 using openly available packages, including NumPy (1.22.2), SciPy (1.7.3), Pandas (1.2.4), neurokit2 (0.2.0), Scikit-learn (1.0.2), and SHAP (0.43.0). Visualization was created using MATLAB R2020a.

Evaluation metrics. To evaluate the performance of the blood pressure prediction using BCG signals, we employ several statistical metrics. Each metric provides a unique perspective on the accuracy and reliability of the predictions. Below are the formulas for each metric:

1. Mean error (ME): This metric calculates the average of the errors between the predicted and actual values. It is defined as:

$$\mathrm{ME} = \frac{1}{n}\sum_{i=1}^{n}(x_i - y_i)$$

where x_i is the predicted value for the ith sample, and y_i is the actual value for the ith sample.

2. Mean absolute error (MAE): This metric computes the average of the absolute differences between the predicted and actual values. It is given by:

$$\mathrm{MAE} = \frac{1}{n}\sum_{i=1}^{n}|x_i - y_i|$$

3. Standard deviation (STD): This metric indicates the amount of variation in the prediction errors. It is calculated as:

$$\mathrm{STD} = \sqrt{\frac{1}{n-1}\sum_{i=1}^{n}(x_i - y_i - \mathrm{ME})^2}$$

4. Pearson correlation coefficient (Corr): This metric measures the linear correlation between the predicted and actual values. It is defined as:

$$\mathrm{Corr} = \frac{\sum_{i=1}^{n}(x_i - \bar{x})(y_i - \bar{y})}{\sqrt{\sum_{i=1}^{n}(x_i - \bar{x})^2}\sqrt{\sum_{i=1}^{n}(y_i - \bar{y})^2}}$$

where $\bar{x}$ and $\bar{y}$ are the mean of the predicted values and actual values, respectively.

5. The receiver operating characteristic (ROC) curves: It is plotted by assessing the trade-offs between sensitivity and specificity across different threshold settings, where the sensitivity and specificity are calculated as (TP: true positive; FN: false negative; TN: true negative; FP: false positive):

$$\mathrm{Sensitivity} = \frac{\mathrm{TP}}{\mathrm{TP}+\mathrm{FN}}, \quad \mathrm{Specificity} = \frac{\mathrm{TN}}{\mathrm{TN}+\mathrm{FP}}$$

The 95% confidence interval (CI) is constructed based on leave-one-out validation results.

Reporting summary

Further information on research design is available in the Nature Portfolio Reporting Summary linked to this article.

Data availability

The main data supporting the results of this study are available within the paper and its Supplementary Information. The public datasets used in this study can be accessed via IEEE Dataport[44]. The labeled dataset generated during the current study is available in the following figshare repository[45].

Code availability

The custom code is available at GitHub[46].

Received: 30 April 2024; Accepted: 6 November 2024;
Published online: 19 December 2024

References

1. Ding, X.-R. et al. Continuous blood pressure measurement from invasive to unobtrusive: celebration of 200th birth anniversary of Carl Ludwig. *IEEE J. Biomed. Health Inform.* **20**, 1455–1465 (2016).
2. Parati, G., Ochoa, J. E., Lombardi, C. & Bilo, G. Assessment and management of blood-pressure variability. *Nat. Rev. Cardiol.* **10**, 143–155 (2013).
3. Boggia, J. et al. Prognostic accuracy of day versus night ambulatory blood pressure: a cohort study. *Lancet* **370**, 1219–1229 (2007).
4. Kario, K. Nocturnal hypertension: new technology and evidence. *Hypertension* **71**, 997–1009 (2018).
5. Kario, K. et al. Nighttime blood pressure measured by home blood pressure monitoring as an independent predictor of cardiovascular events in general practice: the j-hop nocturnal blood pressure study. *Hypertension* **73**, 1240–1248 (2019).
6. Hoshide, S., Kanegae, H. & Kario, K. Nighttime home blood pressure as a mediator of n-terminal pro-brain natriuretic peptide in cardiovascular events. *Hypertens. Res.* **44**, 1138–1146 (2021).
7. Yang, W.-Y. et al. Association of office and ambulatory blood pressure with mortality and cardiovascular outcomes. *JAMA* **322**, 409–420 (2019).
8. Mokwatsi, G. G. et al. Direct comparison of home versus ambulatory defined nocturnal hypertension for predicting cardiovascular events: the Japan morning surge-home blood pressure (j-hop) study. *Hypertension* **76**, 554–561 (2020).
9. Dimsdale, J. E., Coy, T. V., Ancoli-Israel, S., Clausen, J. & Berry, C. C. The effect of blood pressure cuff inflation on sleep a polysomnographic examination. *Am. J. Hypertens.* **6**, 888–891 (1993).
10. Boubouchairopoulou, N., Ntineri, A., Kollias, A., Destounis, A. & Stergiou, G. S. Blood pressure variability assessed by office, home, and ambulatory measurements: comparison, agreement, and determinants. *Hypertens. Res.* **44**, 1617–1624 (2021).
11. Mukkamala, R. et al. Evaluation of the accuracy of cuffless blood pressure measurement devices: challenges and proposals. *Hypertension* **78**, 1161–1167 (2021).
12. Schutte, A. E., Kollias, A. & Stergiou, G. S. Blood pressure and its variability: classic and novel measurement techniques. *Nat. Rev. Cardiol.* **19**, 643–654 (2022).
13. Stergiou, G. S. et al. Methodology and technology for peripheral and central blood pressure and blood pressure variability measurement: current status and future directions–position statement of the european society of hypertension working group on blood pressure monitoring and cardiovascular variability. *J. Hypertens.* **34**, 1665–1677 (2016).
14. Stergiou, G. S. et al. Cuffless blood pressure measuring devices: review and statement by the european society of hypertension working group on blood pressure monitoring and cardiovascular variability. *J. Hypertens.* **40**, 1449–1460 (2022).
15. Ma, Y. et al. Relation between blood pressure and pulse wave velocity for human arteries. *Proc. Natl Acad. Sci. USA* **115**, 11144–11149 (2018).
16. Mukkamala, R. et al. Toward ubiquitous blood pressure monitoring via pulse transit time: theory and practice. *IEEE Trans. Biomed. Eng.* **62**, 1879–1901 (2015).
17. Wibmer, T. et al. Blood pressure monitoring during exercise: comparison of pulse transit time and volume clamp methods. *Blood Press.* **24**, 353–360 (2015).
18. Finnegan, E. et al. Pulse arrival time as a surrogate of blood pressure. *Sci. Rep.* **11**, 22767 (2021).
19. Yavarimanesh, M. et al. Assessment of calibration models for cuffless blood pressure measurement after one year of aging. *IEEE Trans. Biomed. Eng.* **69**, 2087–2093 (2022).
20. Polónia, J., Barbosa, L., Silva, J. A. & Maldonado, J. Different influences on central and peripheral pulse pressure, aortic wave reflections and pulse wave velocity of three different types of antihypertensive drugs. *Rev. Port. Cardiol.* **22**, 1485–1492 (2003).
21. Kelly, R., Millasseau, S., Ritter, J. & Chowienczyk, P. Vasoactive drugs influence aortic augmentation index independently of pulse-wave velocity in healthy men. *Hypertension* **37**, 1429–1433 (2001).
22. Parati, G., Stergiou, G. S., Dolan, E. & Bilo, G. Blood pressure variability: clinical relevance and application. *J. Clin. Hypertens.* **20**, 1133–1137 (2018).
23. Choi, Y., Zhang, Q. & Ko, S. Noninvasive cuffless blood pressure estimation using pulse transit time and Hilbert–Huang transform. *Comput. Electr. Eng.* **39**, 103–111 (2013).
24. Chen, W., Kobayashi, T., Ichikawa, S., Takeuchi, Y. & Togawa, T. Continuous estimation of systolic blood pressure using the pulse

arrival time and intermittent calibration. *Med. Biol. Eng. Comput.* **38**, 569–574 (2000).
25. Cattivelli, F. S. & Garudadri, H. Noninvasive cuffless estimation of blood pressure from pulse arrival time and heart rate with adaptive calibration. In *2009 Sixth International Workshop on Wearable and Implantable Body Sensor Networks* 114–119 (IEEE, 2009).
26. McCarthy, B., O'Flynn, B. & Mathewson, A. An investigation of pulse transit time as a non-invasive blood pressure measurement method. *J. Phys. Conf. Ser.* **307**, 012060 (2011).
27. Jadooei, A., Zaderykhin, O. & Shulgin, V. Adaptive algorithm for continuous monitoring of blood pressure using a pulse transit time. In *2013 IEEE XXXIII International Scientific Conference Electronics and Nanotechnology (ELNANO)* 297–301 (2013).
28. Gordon, J. Certain molar movements of the human body produced by the circulation of the blood. *J. Anat. Physiol.* **11**, 533 (1877).
29. Kim, C.-S. et al. Ballistocardiogram: mechanism and potential for unobtrusive cardiovascular health monitoring. *Sci. Rep.* **6**, 31297 (2016).
30. Carlson, C. et al. Bed-based ballistocardiography: dataset and ability to track cardiovascular parameters. *Sensors* **21**, 156 (2020).
31. Gellman, M. et al. Posture, place, and mood effects on ambulatory blood pressure. *Psychophysiology* **27**, 544–551 (1990).
32. Kawano, Y. Diurnal blood pressure variation and related behavioral factors. *Hypertens. Res.* **34**, 281–285 (2011).
33. Medical, C. Number of iot connected devices worldwide 2019-2030. https://caretakermedical.net/ (2024).
34. Zou, G. Confidence interval estimation for the bland–altman limits of agreement with multiple observations per individual. *Stat. Methods Med. Res.* **22**, 630–642 (2013).
35. Stergiou, G. S. et al. A universal standard for the validation of blood pressure measuring devices: association for the advancement of medical instrumentation/european society of hypertension/international organization for standardization (aami/esh/iso) collaboration statement. *Hypertension* **71**, 368–374 (2018).
36. IEEE standard for wearable cuffless blood pressure measuring devices. In *IEEE Std 1708-2014* 1–38 (IEEE, 2014).
37. IEEE standard for wearable, cuffless blood pressure measuring devices - amendment 1. In *IEEE Std 1708a-2019 (Amendment to IEEE Std 1708-2014)* 1–35 (IEEE, 2019).
38. O'Brien, E. et al. The british hypertension society protocol for the evaluation of blood pressure measuring devices. *J. Hypertens.* **11**, S43–S62 (1993).
39. Pickering, T. G. et al. Recommendations for blood pressure measurement in humans and experimental animals: part 1: blood pressure measurement in humans: a statement for professionals from the subcommittee of professional and public education of the american heart association council on high blood pressure research. *Circulation* **111**, 697–716 (2005).
40. Kim, C.-S., Carek, A. M., Inan, O. T., Mukkamala, R. & Hahn, J.-O. Ballistocardiogram-based approach to cuffless blood pressure monitoring: proof of concept and potential challenges. *IEEE Trans. Biomed. Eng.* **65**, 2384–2391 (2018).
41. Inan, O. T. et al. Ballistocardiography and seismocardiography: a review of recent advances. *IEEE J. Biomed. Health Inform.* **19**, 1414–1427 (2014).
42. Giovangrandi, L., Inan, O. T., Wiard, R. M., Etemadi, M. & Kovacs, G. T. Ballistocardiography—a method worth revisiting. *Annu. Int. Conf. IEEE Eng. Med. Biol. Soc.* **2011**, 4279–4282 (2011).
43. Huang, Y. et al. Nf-heart: a near-field non-contact continuous user authentication system via ballistocardiogram. *Proc. ACM Interact. Mob. Wearable Ubiquit. Technol.* **7**, 1–24 (2023).
44. Carlson, C. Bed-based ballistocardiography dataset. https://ieee-dataport.org/open-access/bed-based-ballistocardiography-dataset (2024).
45. Labeled data. https://doi.org/10.6084/m9.figshare.26490769.v1 (2024).
46. Bcg2bp. https://github.com/Island520/BCG2BP (2024).

Acknowledgements

This research is supported in part by Guangdong Provincial Key Lab of Integrated Communication, Sensing and Computation for Ubiquitous Internet of Things (No.2023B1212010007), China NSFC Grant U2001207, the Project of DEGP (No.2023KCXTD042 and 2021ZDZX1068), the Guangzhou Science and Technology Program (2024A03J074, 2023A03J0286, and 2024A03J0927), RGC under Contract CERG 16206122, 16204523, AoE/E-601/22-R, R6021-20, and Contract R8015. Furthermore, the authors want to thank Ms. Xinwen Zhang for her help and support in the data collection.

Author contributions

Y.H. conceived the original idea, designed the research, and wrote the initial draft of the manuscript. C.L., J.P., W.L., and C.Y. designed the sensor mat and the hardware system. Y.H., J.P., and L.C. performed software design and software validation. Y.H. and L.C. contributed to the model implementation and data analysis. Y.H., Q.H., and Y.S. contributed to the data collection and experimental works with support from J.T., W.J., and W.C. K.W. and Q.Z. designed the experiment protocol, supervised the study, and provided strategic guidance.

Competing interests

The authors declare no competing interests.

Additional information

Supplementary information The online version contains supplementary material available at https://doi.org/10.1038/s44172-024-00326-w.

Correspondence and requests for materials should be addressed to Weibin Cheng, Kaishun Wu or Qian Zhang.

Peer review information *Communications Engineering* thanks the anonymous reviewers for their contribution to the peer review of this work. Primary Handling Editors: Chaoran Huang and Anastasiia Vasylchenkova.